5

Nitrogen doped twisted graphene

Ivan V. Komissarov[1,3], Nikolai G. Kovalchuk[1], Algirdas Lazauskas[2], Mindaugas Andrulevičius [2], Sigitas Tamulevičius[2], Nikolai I. Kargin[3] and Serghej L. Prischepa[*1,3]

[1]Belarusian State University of Informatics and Radioelectronics, P. Brovka str. 6, Minsk 220013, Belarus.
[2]Institute of Materials Science, Kaunas University of Technology, K. Baršausko str. 59, Kaunas 51423, Lithuania.
[3]National Research Nuclear University "MEPHI", Kashirskoe Highway 31, Moscow 115409, Russia.
[*]Corresponding author

Outline

Introduction

The single layer graphene (SLG) shows exceptional electronic properties making it one of the most advanced material nowadays. Due to the high charge carrier mobility [1] it has huge functional ability in many applications, especially in high frequency electronics. The electronic properties of graphene layers depend on staking order [2]. For example, Bernal-stacked graphene shows a quadratic energy-momentum dispersion near the Dirac point due to the strong interlayer interaction [3,4]. Moreover, contrary to the monolayer graphene in Bernal-stacked graphene multilayers, electron backscattering is allowed [5]. However, when the layers of graphene are not strongly electronically coupled, this scenario is not always realized. Indeed, for turbostratic graphite, where the Bernal stacking is destroyed, even for very large number of layers, the unique properties of graphene can be preserved [6]. Double (triple) layer turbostratic graphite is also known as twisted graphene (TG). This term reflects the fact that both the electronic and structural properties of double layer graphene can be well described by the in-plane rotation angle θ between the graphene layers, see Figure 5.1.
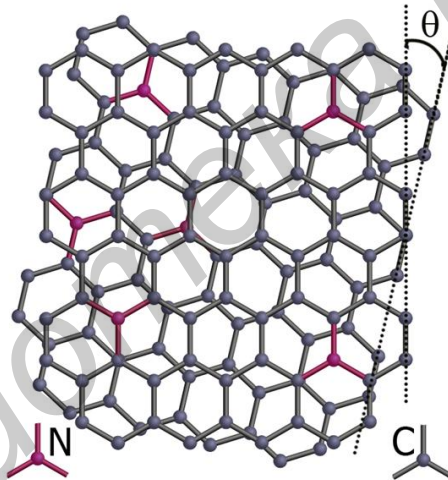

FIGURE 5.1
Twisted graphene and angle θ between two graphene layers. Graphene is doped by nitrogen atoms

Many theoretical and experimental studies have focused on the unique properties of TG [7]. In particular, it was demonstrated that for angles $\theta > 10°$, the layers are electronically decoupled, and the low-energy band structure looks like a simple superposition of the Dirac cones of the individual graphene planes [8]. Moreover, the Fermi velocity reaches the value for SLG (10^6 m/s) for $\theta > 10°$, and drastically decreases for $\theta < 5°$ [8]. In addition, one of the most attractive characteristic of the TG is the pair of logarithmic divergence in the density of states, known as the van Hove singularities (vHS), which are formed due to the overlap of the Dirac cones in the k-space. The energy of these singularities is symmetrically (within ± 1 eV) built up with respect to the Dirac point. The energy separation of the vHS increases with the angle θ [9,10]. Many other interesting phenomena are associated with the TG, like the enhanced optical absorption [11,12], non-dispersive flat bands at

the charge neutrality point related to confinement [13,14], enhanced photochemical reactivity [15], etc.

The controlled injection of defects, which cause strain, is an extra degree of freedom in addition to the number of layers. This may account for the unique properties of TG. In particular, it was shown that the strained TG bilayer could be an ideal platform for the realization of the high-temperature zero-field quantum valley Hall effect [16]. From a practical point of view, the band gap opening in the electronic structure of graphene is quite attractive. It is expected that this will result in a new approach for application of graphene in digital electronics. It was also theoretically predicted that, in TG with small uniaxial strain, which comprises only a few percent, a finite conduction gap as large as hundreds of meV can be obtained [17]. Thus, the study of the defects impact on the TG properties is quite motivating topic from both fundamental and applied aspects.

TG can be obtained by different methods, e.g., by means of graphene folding, graphene layers stacking, thermal decomposition of SiC [18] or chemical vapor deposition (CVD) on metal catalysts [19,20]. Generally speaking, CVD is one of the most common methods to obtain large area and high quality graphene [21]. Moreover, TG may be grown at ambient pressure applying atmospheric pressure CVD (APCVD) [19]. The use of different hydrocarbon sources to explore the growth mechanism and properties of TG is a hot topic nowadays. Generally, methane (CH_4) is the most common hydrocarbon used in the CVD process to grow graphene. However, the use of other hydrocarbons rather than CH_4 compounds is a challenging task. It may offer the possibility to tune the growth process and to pave the way to graphene synthesis with desirable parameters, such as type of defects and their concentration.

The generally accepted pathway of graphene growth by the APCVD on the catalyst is as follows. Carbon species diffuse through the boundary layer and reach the surface, where they are adsorbed and decomposed to form an active carbon species, which diffuse onto the surface of the catalyst or into the catalyst close to the surface and form the graphene lattice. Inactive species (such as hydrogen) are desorbed from the surface, forming molecular hydrogen, diffuse away from the surface through the boundary layer and are eventually swept away by the bulk gas flow [22].

All of the above stages depend essentially on the hydrocarbon precursor [23]. At this point, a precursor that has similar chemical properties but different molecular mass looks attractive for deeper understanding of the graphene growth kinetics. One of such candidates is n-decane ($C_{10}H_{22}$), a member of the homologous series of alkane hydrocarbons. n-decane has a molecular mass on the order of magnitude greater than that of methane that influences the growth kinetics of graphene. As a representative of n-alkanes, n-decane forms during thermal decomposition chains of radicals with high reactive nature. This provokes numerous chemical reaction pathways and promotes doping. In fact, the CVD makes it possible to dope graphene by nitrogen *in situ*, which not only tolerates the ground state of graphene via additional electrons but also introduces a strain to graphene because of the difference in ionic radii [24]. The radicals resulting from the decomposition of n-decane, could lead to the decomposition of the nitrogen molecule, which in fact has one of the strongest binding energy. The resulting atomic nitrogen can be embedded into the graphene lattice. The nitrogen doping of graphene causes the band gap opening in it [25]. Thus, the nitrogen doped TG looks as a very promising object to study fundamental aspects of the strain induced behavior. In this chapter, we present experimental conditions at which the APCVD growth of large area nitrogen doped TG can be realized utilizing n-decane as a precursor in the presence of nitrogen flow.

Samples Fabrication and Experimental Technique

Synthesis and transfer

Custom-made APCVD facility with 14 mm diameter tubular quartz reactor was employed for the experiment. Polycrystalline copper foil (99.9 % purity proved by the EDX study) having a thickness of 60 μm was used as the catalyst. Prior to the APCVD, the foil was electrochemically polished for 5 min in 1M phosphoric acid at a bias voltage of a 2.3 V. The 35×45 mm^2 sample was placed in the middle of the reactor. One side of the copper foil covered the inner wall of the reactor. Copper foil was annealed for one hour at the temperature of 1050 °C in the presence of N_2 and H_2 gas flow with the rate of 100 and 150 cm^3/min, respectively. The purity of the nitrogen gas was 99.95 %. We utilized commercial hydrogen generator GVCh-12D as a H_2 source. The resulting purity of the hydrogen gas was 99.99 %. The temperature was controlled by a thermocouple placed inside the heating block, next to the reactor wall.

In this chapter, we present the results related to two samples: sample A and sample B. Sample A was prepared at the temperature of 1050 °C in the presence of N_2 and H_2 gas flow with the rates of 100 and 60 cm^3/min, respectively. Sample B was prepared under similar conditions, except the H_2 gas flow rate, - it was reduced to 6 cm^3/min. The decane was introduced into the tubular quartz reactor via barbotage system for 30 min. The feeding rate of decane was estimated to be 4 μl/min (for both samples). Afterwards, the tubular quartz reactor was cooled at a rate of 50 °C/min in the presence of N_2 gas flow. The obtained properties of samples A and B are typical for samples synthesized under similar conditions.

The transfer of graphene from the original catalyst to the arbitrary substrate without deteriorating the crystallinity of graphene is still a challenging task [26]. Currently, there are two main approaches to the transfer of graphene. The first one consists in a mechanical exfoliation, which imposes severe mechanical uncontrolled defects in the sample. The most common and preferable is a wet-chemical etching of the catalyst (substrate). Usually a poly(methylmethacrylate) (PMMA) scaffold is applied to coat the graphene surface and support it during the catalyst consumption, underside contaminant cleaning, placement on the destination substrate. However, the PMMA removal from graphene after the film transfer that is followed by high temperature Ar/H_2 forming gas annealing [27], O_2 based annealing [28], and *in situ* annealing [29], deteriorates the graphene crystallinity. Additionally, these processes are operated at high temperatures, which restricts the application of graphene, including its use in flexible electronics and biomolecule encapsulation [30]. Therefore, in this work we employed a wet-chemical room temperature transfer process onto SiO_2(598 nm)/Si substrates without using any polymer support. It was performed in two steps.

First, one side (the one that was next to the reactor wall) of copper foil was treated for 3 min in a solution of H_2NO_3 and H_2O mixed in a volume ratio of 1:3, and then the copper foil was totally dissolved in a water solution of $FeCl_3$. Graphene film was gently washed several times in a bath with distilled water prior to the transfer onto the substrate.

Characterization

Graphene samples were analyzed by Raman spectroscopy technique. For that, we utilized the Nanofinder HE, with 532 nm and 473 nm excitation wavelengths, and Confotec NR500 confocal micro-Raman spectrometer, with 473 nm excitation wavelength. The spectral resolution was about 3 cm^{-1} for both spectrometers. Three-dimensional scanning laser confocal Raman microscope Confotec NR500 provides the acquisition of two kinds of images within a single scan: a Rayleigh

image, using laser light reflected from a sample, and a spectral image by Raman scattering. More details about the laser beam size and spectra accumulation time are presented further in the text. Thermo Scientific ESCALAB 250Xi spectrometer with a monochromatic Al Kα radiation ($h\nu$ =1486:6 eV) was used for X-ray photoelectron spectroscopy (XPS) measurements. Base pressure in the analytical chamber was better than 2×10^{-7} Pa. The 20 eV and 40 eV pass energy values of a hemispherical electron energy analyzer were used for survey and detailed spectra acquisition, respectively. Energy scale of the system was calibrated according to Au $4f_{7/2}$, Ag $3d_{5/2}$ and Cu $2p_{3/2}$position of the peaks. Original ESCALAB 250Xi Avantage software was used for peaks deconvolution and fitting procedure using a sum of Lorentzian-Gaussian (70:30) functions. The samples were analyzed as received, no surface cleaning procedure was applied. Finally, the transmittance spectra were acquired using the PROSCAN MC-121 spectrometer.

Results of Raman Study

The optical images of samples A and B on a copper foil are shown in Figure 5.2a and Figure 5.2b, respectively. The surface of sample A contains randomly distributed hexagonally-shaped spots (brighter areas), while the surface of sample B looks relatively homogeneous.
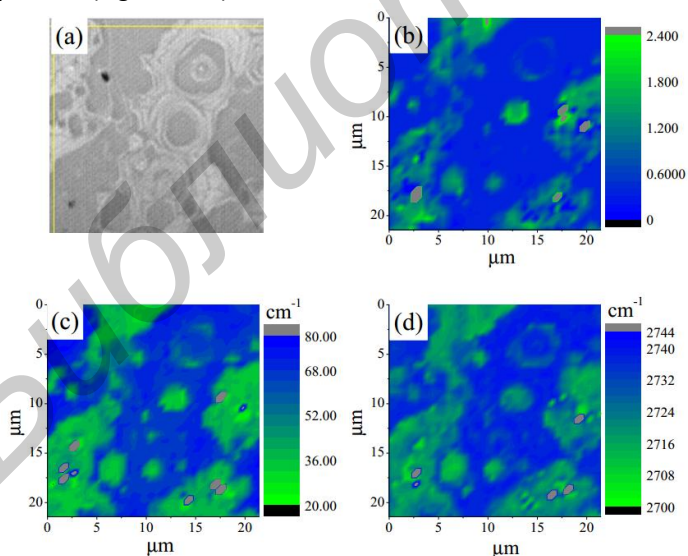

FIGURE 5.2
Optical images for (a) sample A, (b) sample B as deposited on copper foil

Important information about the structure of graphene can be obtained from the Raman investigations. Indeed, the resonance nature of Raman spectra in graphene makes them a versatile tool for studying both structural and electronic properties [31]. In Figure 5.3a we show the individual Raman spectrum of sample A acquired in the darker part, see Figure 5.2a. Figure 5.3b presents the Raman spectrum characteristic of sample B. In the insets to Figures 5.3a and 5.3b the 2D peaks are shown revealing the symmetry of the 2D band. The latter indicates the weak interlayer interaction, which will be discussed later.
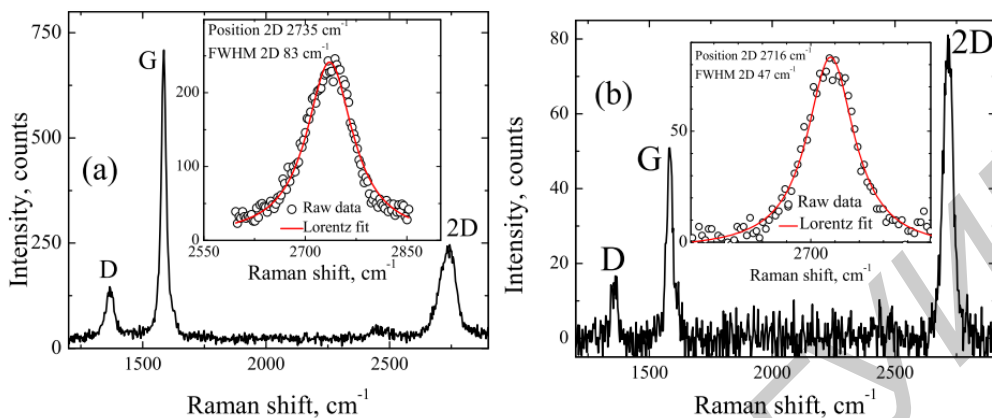
FIGURE 5.3

Individual Raman spectrum for (a) sample A, (b) sample B on copper foil acquired at a laser wavelength of 473 nm. Insets: Measured 2D peak (symbols) with Lorentz fit (line)

In Figure 5.4a we demonstrate the Rayleigh image of sample A transferred to SiO_2/Si substrate. Raman mapping (1600 points) was performed for the same sample area as in Figure 5.4a. A single spectrum was accumulated for 1 s with a laser excitation wavelength of 473 nm and a beam diameter of about 600 nm. The results of this study are presented in Figure 5.4(b-d) and Figure 5.5, in which we show the relation between the intensities of the 2D and G bands, I_{2D}/I_G (Figure 5.4b), full width at the half maximum (FWHM) map of the 2D band (Figure 5.4c), the 2D band map (Figure 5.4d) and corresponding Raman mapping histograms for the G band position (Figure 5.5a), I_{2D}/I_G ratio (Figure 5.5b), FWHM of the 2D band (Figure 5.5c) and, finally, histogram for the 2D band position (Figure 5.5d).

FIGURE 5.4

(a) The Rayleigh image. (b) $I_{2D}=I_G$ ratio map. (c) FWHM map of the 2D band. (d) 2D band position map. All data are for sample A on SiO_2=Si substrate acquired with a laser excitation wavelength of 473 nm. Color coding represents the amplitude of measured values

The correlation between the Rayleigh image (Figure 5.4a) and I_{2D}/I_G ratio (Figure 5.4b) is clearly seen. The domains with the I_{2D}/I_G ratio greater than 0.6 correspond to the dark spots in the optical image. The FWHM map of the 2D band (Figure 5.4c) and corresponding histogram (Figure 5.5c) suggest that a significant part of the sample is associated with the domains in which this parameter is less than 40 cm^{-1}, which is typical for a SLG [32]. However, the Raman map of the 2D band positions (Figure 5.3d) and corresponding histogram (Figure 5.4d) indicate that only negligible part of the film surface is associated with the values smaller than 2710 cm^{-1}. It is important to note, that the 2D band position of graphene transferred on SiO$_2$ and measured with the 473 nm laser excitation wavelength should be equal to 2703 cm^{-1} [33]. It means that the position of the 2D band is blue shifted in sample A. The significant blue shift in the position is also observed for the G band (Figure 5.5a), 1585 cm^{-1} and 1588 cm^{-1} against 1580 cm^{-1} for SLG [34].
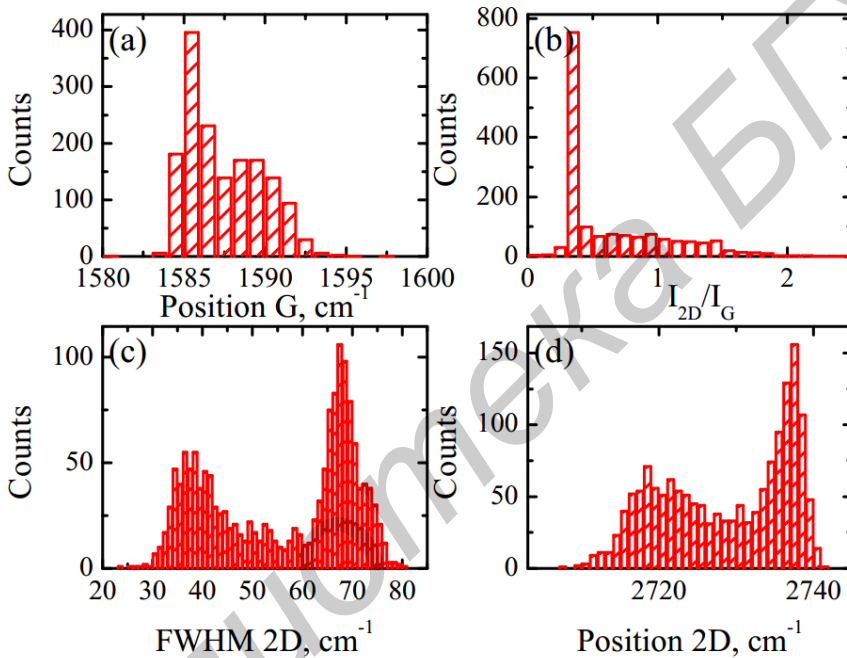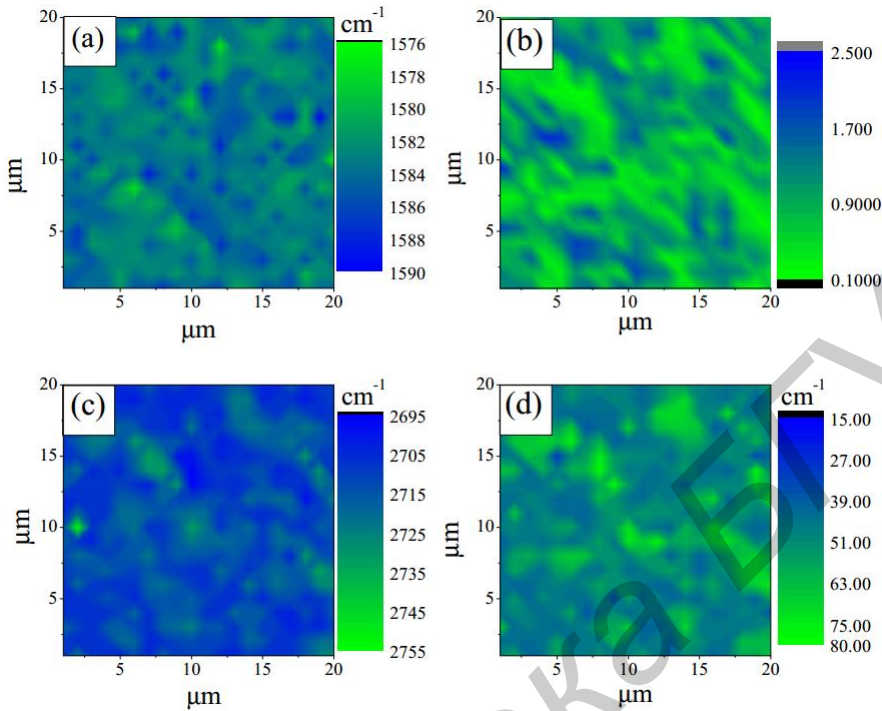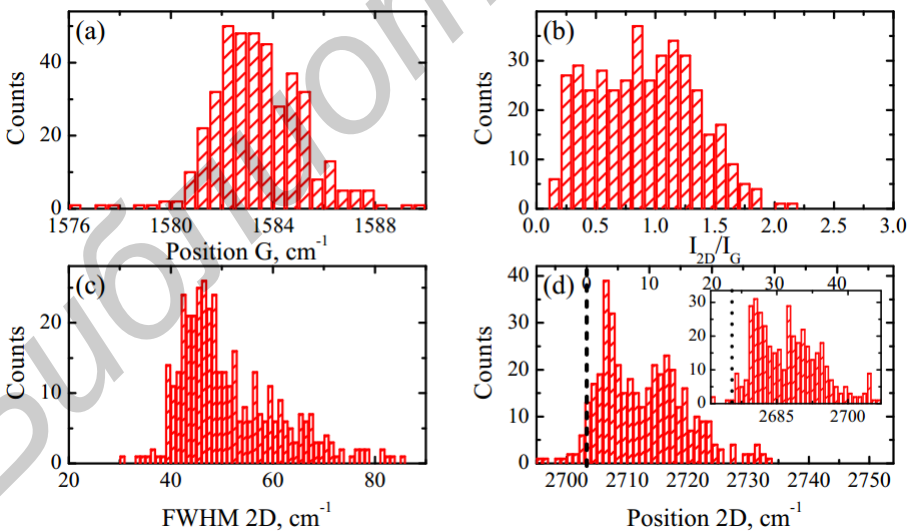

FIGURE 5.5
Raman mapping histograms for sample A on SiO$_2$/Si substrate as obtained from Raman maps of Figure 5.4. (a) G band position. (b) I$_{2D}$=I$_G$. (c) FWHM of the 2D band. (d) 2D band position

Figure 5.6(a-d) shows Raman maps (400 points) of sample B transferred on SiO$_2$/Si substrate. Despite the lower number of points compared to sampleA, the main characteristic features of the spectra are well understood and distinguishable. The corresponding histograms are presented in Figure 5.7(a-d). A single Raman spectrum was accumulated for 10 s with a laser wavelength of 473 nm and a beam diameter of about 600 nm. The I_{2D}/I_G ratio map (Figure 5.6b) shows the existence of domains with relatively uniform distribution. Moreover, correlation between the I_{2D}/I_G ratio (Figure 5.6b) and 2D band position (Figure 5.6d) maps is observed.

The same area of sample B was analyzed with a different laser excitation wavelength, 532 nm, utilizing the same conditions of laser beam as for 473 nm. By analogy with the previous Raman maps, the non-monotonic distribution of mapped values was observed. As an example, in the inset to Figure 5.7d we show the histogram for the 2D band position obtained with a 532 nm excitation wavelength. The similarity of the results for two different wavelengths is obvious.

FIGURE 5.6
Raman maps of sample B on SiO$_2$/Si substrate acquired at laser excitation wavelength of 473 nm. (a) G band position. (b) I_{2D}/I_G ratio. (c) FWHM of the 2D band. (d) 2D band position

FIGURE 5.7
Raman mapping histograms for sample B on SiO$_2$/Si substrate as obtained from Raman maps of Figure 5.6. (a) G band position. (b) I_{2D}/I_G. (c) FWHM of the 2D band. (d) 2D band position. Inset: 2D band as measured for the laser excitation wavelength of 532 nm. The vertical dashed lines on panel (d) show the position of the 2D band of SLG on SiO$_2$ according to Ref. [30]

Splitting of Raman Data

In many aspects, the theory of Raman scattering in graphene is very well elaborated and quantitative analysis of Raman spectra parameters provides sufficient information about structural and electrical properties of graphene. For example, analysis of the line shape of the 2D band along with its position can provide important information about the number of layers in graphene [35]. From the G band position the carrier concentration can be obtained with high accuracy [36]. Finally, analysis of the I_D/I_G ratio is getting to be a common method for the point defect concentration evaluation [37,38].

From Raman spectroscopy applied in the current research it follows that the non-monotonic distribution is inherent for almost all data histograms presented in the section Results. For instance, two sharp maxima are observed in the FWHM of the 2D band histogram of sample A (Figure 5.5c), at approximately 38 cm^{-1} and 67 cm^{-1}, respectively. It suggests the presence within the same sample of at least two graphene "systems" with quite different number of layers. Indeed, the presence of two maxima in the 2D position distribution (Figure 5.4d) is in good accordance with the observation of thicker and thinner domains in optical images (Figure 5.2a). Consequently, it is reasonable to analyze Raman spectra separately applying the criterion for data belonging to a particular peak.

Following this idea, we split the Raman data of sample A into two sets, one of which contains data where the 2D FWHM values are smaller than 50 cm^{-1} and another is for data with the 2D FWHM greater than 50 cm^{-1}.
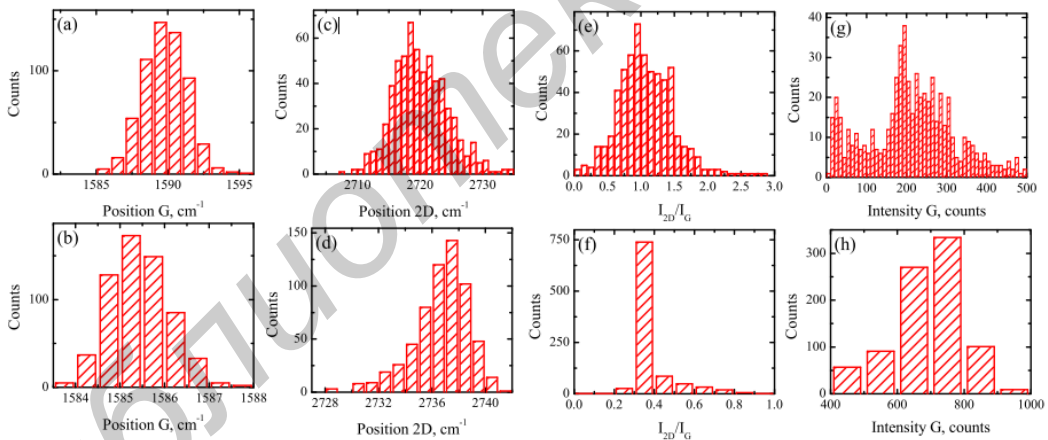

FIGURE 5.8
Re-plotted histograms of sample A on SiO$_2$/Si substrate for laser excitation wavelength of 473 nm using 2D FWHM = 50 cm^{-1} as a splitting criterion. (a) and (b) G band position. (c) and (d) 2D band position. (e) and (f) I_{2D}/I_G ratio. (g) and (h) I$_G$ value. Data shown in (a), (c), (e) and (g) plots are for 2D FWHM < 50 cm^{-1}. Data shown in (b), (d), (f) and (h) plots are for 2D FWHM > 50 cm^{-1}

Histograms re-plotted per this criterion are shown in Figure 5.8(a-h). Data for the 2D FWHM smaller than 50 cm^{-1} are shown in Figures 5.8a, 8c, 8e and 8g, while data for the 2D FWHM greater than 50 cm^{-1} are presented in Figures 5.8b, 8d, 8f and 8h. It is clearly seen that the histograms exhibit relatively monotonic distribution with one distinct maximum. The I_{2D}/I_G ratio has the maximum with the value roughly equal to unit for the Raman data with the 2D FWHM smaller than 50 cm^{-1} (Figure 5.8e). Domains of sample A, which correspond to this set of Raman data can be attributed

to a single or double layer graphene. According to Costa et al. [33], the single layer graphene on SiO$_2$ substrate for laser excitation wavelength of 473 nm should exhibit the 2D band position at 2703 cm^{-1}. The significant blue shift for the 2D band position (2718 cm^{-1}) could be caused by double layer structure of graphene [35] and/or doping effect [24]. The G band position at 1590 cm^{-1} (Figure 5.8a) is also blue shifted from the accepted standard value of 1580 cm^{-1} for the undoped graphene [34]. Further, Raman data with the 2D FWHM greater than 50 cm^{-1} (Figures 5.8b, 8d, 8f and 8h) also exhibit rather monotonic distribution of values with a single maximum. The G band position together with the blue shifted 2D position and a sharp peak at 0.3 of the I_{2D}/I_G ratio allow associating these domains of sample A with a larger thickness. Indeed, the significant difference of the G band intensity between these two sets (Figures 5.8g and 5.8h) confirms this statement.

As we already mentioned above, the nonmonotonic distribution is a characteristic feature of the obtained histograms. Thus, the splitting of the Raman spectra could be based on different parameters, I_{2D}/I_G, FWHM 2D, position of the 2D or G band. For sample A we performed the splitting procedure following different parameters (this result is not shown here). The obtained results are in reasonable agreement with each other. However, for sample B the splitting procedure may leave some nonmonotonicity in histograms associated with the thicker fraction of the film.

Figure 5.9 presents histograms for sample B on SiO$_2$/Si substrate after splitting procedure where the splitting was based on another criterion, namely, the 2D band position with the splitting value of 2712 cm^{-1} (Figure 5.9(a-h)). At that it was used the same laser excitation wavelength as for sample A (473 nm). Data for the 2D band position smaller than 2712 cm^{-1} are presented in Figures 5.9a, 9c, 9e and 9g, while data for the 2D band position greater than 2712 cm^{-1} are shown in Figures 5.9b, 9d, 9f and 9h. All distributions presented in the top panel of Figure 5.9 are monotonic and the values of FWHM 2D, I_{2D}/I_G, allow associating domains with the 2D band position smaller than 2712 cm^{-1} with the SLG [39].
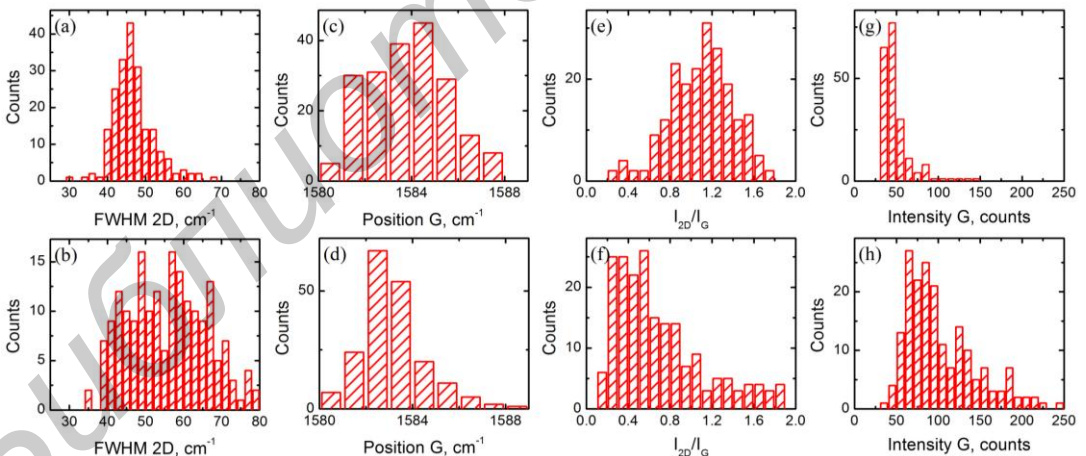

FIGURE 5.9

Re-plotted histograms of sample B on SiO$_2$/Si substrate for laser excitation wavelength of 473 nm using the 2D band position of 2712 cm^{-1} as a splitting criterion. (a) and (b) FWHM of the 2D band. (c) and (d) G band position. (e) and (f) I_{2D}/I_G ratio. (g) and (h) I_G value. Data shown in (a), (c), (e) and (g) plots are for the 2D band position than smaller 2712 cm ^{1}. Data shown in (b), (d), (f) and (h) plots are for the 2D band position greater than 2712 cm^{-1}

Almost two times difference in the G band intensities (see Figure 5.9g Figure 5.9h) could relate histograms presented in the bottom panel of Figure 5.9 to the double layer graphene fraction [40]. However, in contrast to the SLG, the double layer fraction has rather non-monotonic distribution of FWHM2D with significant part of it below 50 cm^{-1}. To verify impact of the splitting criteria on resulting histograms we perform another splitting procedure. Since G band position is sensitive to the number of layers [40], we usethe G band position as a criterion with the value of 1584.25 cm^{-1} (see Figure 5.7a). Data for the G band position greater than 1584.25 cm^{-1} are presented in Figures 5.10a, 10c, 10e and 10g, while data for the G band position smaller than 1584.25 cm^{-1} are shown in Figures 5.10b, 10d, 10f and 10h. As in the previous case the top panel contains manly monotonic distribution whereas the bottom panel contains non-monotonic distribution. Some smearing of distribution is related to the overlap of distributions which is caused by the SLG and double layer fractions and relatively low spectral resolutions of our measurements. However, the difference in the G band intensity between the SLG and double layer fractions is still remaining, meaning that smearing has deeper physical nature which we discuss in the section "Twisted graphene".
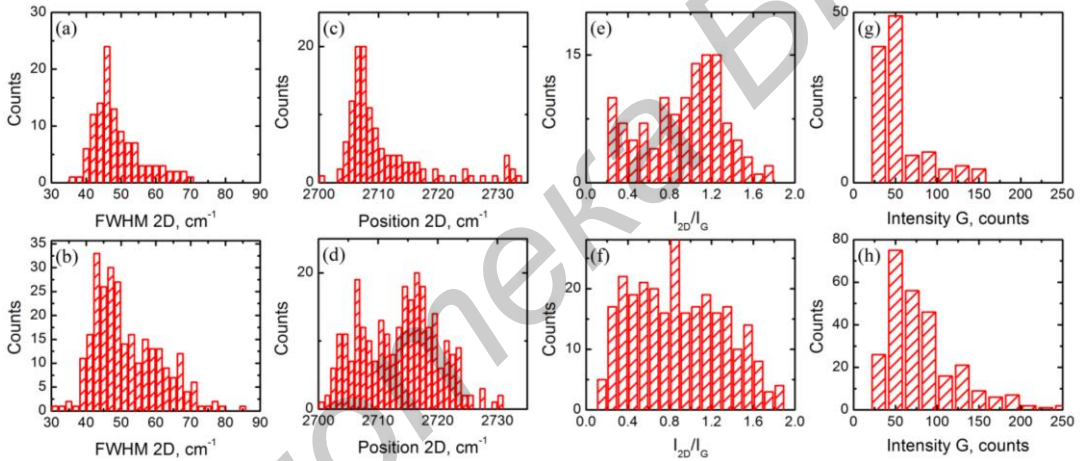

FIGURE 5.10
Re-plotted histograms of sample B on SiO$_2$/Si substrate for laser excitation wavelength of 473 nm using the G band position of 1584.25 cm^{-1} as a splitting criterion. (a) and (b) FWHM of the 2D band. (c) and (d) 2D band position. (e) and (f) I_{2D}/I_G ratio. (g) and (h) I_G value. Data shown in (a), (c), (e) and (g) plots are for the 2D band position greater than 1584.25 cm^{-1}. Data shown in (b), (d), (f) and (h) plots are for the G band position smaller than 1584.25 cm^{-1}

XPS Results

In this section, we carry out the comparison of the parameters of Raman spectra which we attribute to the SLG domains in samples A and B (473 nm excitation wavelength). The maxima of the G band position distribution for the SLG fraction of sample A and B are centered at $\approx$1590 cm^{-1} (Figure 5.8a) and$\approx$ 1585 cm^{-1} (Figure 5.9c), respectively. The maxima of the I_{2D}/I_G ratio are centered at $\approx$1 (Figure 5.8e) and $\approx$ 1.2 (Figure 5.9e) for samples A and B, correspondingly.
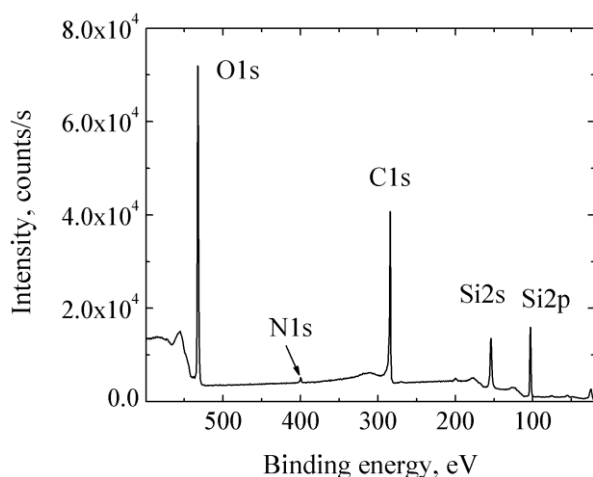
FIGURE 5.11
XPS survey spectrum of sample B

Both these facts indicate that sample A has higher carrier concentration with respect to sample B [36,41]. Considering that for both samples the substrate material, transfer method and conditions of store were the same, it is reasonable to suppose that the main source of the charge may be originated from doping during the growth. Since we use nitrogen as a carrier gas, the probability of this scenario could be high. XPS results can give useful qualitative and quantitative information about graphene doping. Thus, to check the importance of nitrogen doping we performed exhaustive XPS study of both samples.

In Figure 5.11 we show the XPS survey spectrum of the studied sample B transferred on SiO_2/Si substrate. The survey spectrum for sample A (not shown here) looks similar as for sample B. The main core level peaks for carbon, nitrogen, silicon and oxygen are indicated. It is important to note, that due to small thickness of samples the contribution from substrate with strong silicon and oxygen signals was detected. The quantified surface atomic concentrations determined by XPS for samples A and B are summarized in Table 5.1. Figures 5.12a and 5.12b present the high resolution XPS for N1s spectrum of samples A and B, respectively, in which the spectra could be fitted to two components of the binding energy (E_b), namely at E_b = 399.7 eV and 402.1 eV (sample B) (E_b = 401.8 eV (sample A)). Peak at E_b = 399.7 eV observed for both samples is related to the adsorbed nitrogen. The position of the adsorbed nitrogen was quantified by the measurement on the bare substrate area, see inset of Figure 5.12a, indicating that nitrogen dope both samples with a single status. From literature, it is known that it is rather difficult to associate the binding energy with the specific configuration of nitrogen and usually it requires additional structural measurements. Indeed, the energy range 398 – 404 eV can be related to the different nitrogen configurations, such as pyridine-type, pyrrolic-type, graphite-type, and pyridine N-oxide (see, e.g., [42]). We cannot exclude also the formation of very stable nitrile CN bond (sp configuration) [43]. Based only on the XPS data we cannot make unambiguous assignment concerning nitrogen configuration. For example, the binding energy for graphitic nitrogen is varied between 400.0 eV [44] and 402.7 eV [45]. However, two solid conclusions can be announced from the obtained XPS data. (i) nitrogen is incorporated into graphene in a single status; (ii) the concentration of nitrogen associated with the energy of about $E_b \approx 402$ eV is greater for sample A. We would like to emphasize that these observations are consistent with the data of Raman spectroscopy, from which it follows that the G band blue shift is greater for sample A.

TABLE 5.1
Quantified surface atomic concentrations for samples A and B on SiO$_2$/Si substrate as obtained from the XPS study

Sample	Atomic concentration, %		
	C	N(399.74 eV)	N(~402 eV)
A	98.4	0.6	1.00
B	97.6	1.99	0.41

Comparative analysis of the defect concentration from the XPS and Raman data

The XPS measurements provide atomic concentration of nitrogen in studied samples, see Table 5.1. For further discussion, it is more suitable to convert atomic concentration into the surface concentration. For sample B the nitrogen atomic concentration is ~ 0.4%, meaning about one nitrogen atom per 250 carbon atoms. Taking into account the surface concentration of carbon atoms in graphene, ~ 3.8×10^{15} cm^{-2}, the average surface concentration of the nitrogen atoms in sample B can be evaluated as $n_N \approx$ 1.5 x10^{13} cm^{-2}.
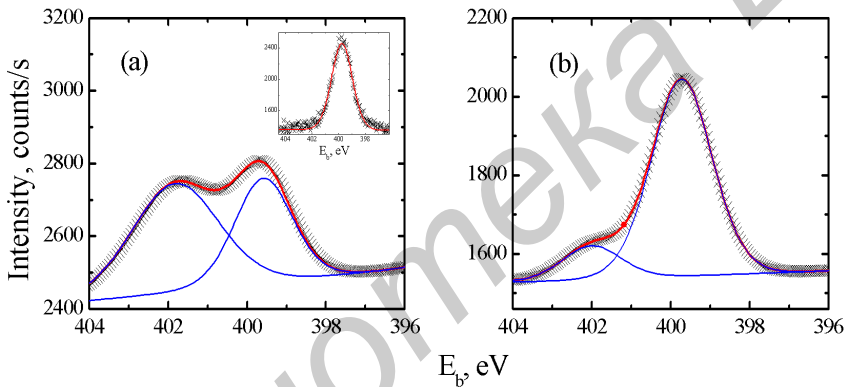
FIGURE 5.12
High resolution N1s XPS spectra of samples on SiO$_2$/Si substrate. (a) Raw data for sample A (black crosses). Blue line is the result of the fitting procedure. Red line corresponds to the envelope of the fitted peaks. Inset: N1s XPS spectrum of a bare substrate (black symbols) together with the fitting curve (red). (b) Raw data for sample B (black crosses). Blue lines are the result of the fitting procedure. Red line corresponds to the envelope of the fitted peaks. Inset: XPS survey spectrum

On the other hand, the Raman integral intensity ratio I_D/I_G provides information about the concentration of point defects *n* [38],

(1) $n(cm^{-2}) \approx 7.3 \times 10^9 E_{laser}^4 \left(\frac{I_D}{I_G}\right)$.

Using from the experiment $I_D/I_G \approx 1$, and the energy of laser $E_{laser} \approx$ 2.33 eV, we get
$n \approx 2.2 \times 10^{11}$ cm^{-2}.

The reason for lower defect density compare to the n_N value may be the following. The nitrogen atoms could be located in such configuration that almost does not affect the I_D value. In particular, the pyrrolic nitrogen due to the symmetry breaking of hexagon rings should have strong impact on the intensity of the D band and cannot be considered as the main type of defect in the studied films.

Twisted Graphene

Now we focus on the Raman data associated with the double layer graphene.In Figure 5.13 we plot selected spectraassociated withthe double layer (red line) and SLG (black line) sets, acquired with different excitation wavelength, 473 nm and 532 nm, for the top and bottom panels respectively. For the double layer spectra shown in Figure 5.13a and Figure 5.13c one may notice 2…3 times enhancement ofthe 2D band intensity and its blue shift as compared to the SGL spectra, whereas FWHMs of the 2D band remain the same, smaller than 50 cm^{-1}. Theseresults could be attributed to the twisted double layer graphene with the rotation angle $\theta > 10^{o}$ [46,47].

Moreover, as we pointed out in the Introduction, the most attractive feature of the TG electronic structure is presence of the vHS. In Raman spectroscopy, the presence of the vHS yields the G-resonance [46]. It consists in more than one order of magnitude enhancement of the G band intensity when the excitation energy fits the vHS energy difference. Indeed, the domains with the G intensity with an order of magnitude higher with respect to that of the SGL were observed for both laser excitation wavelengths, 532 nm (Figure 5.13b) and 473 nm (Figure 5.13d).
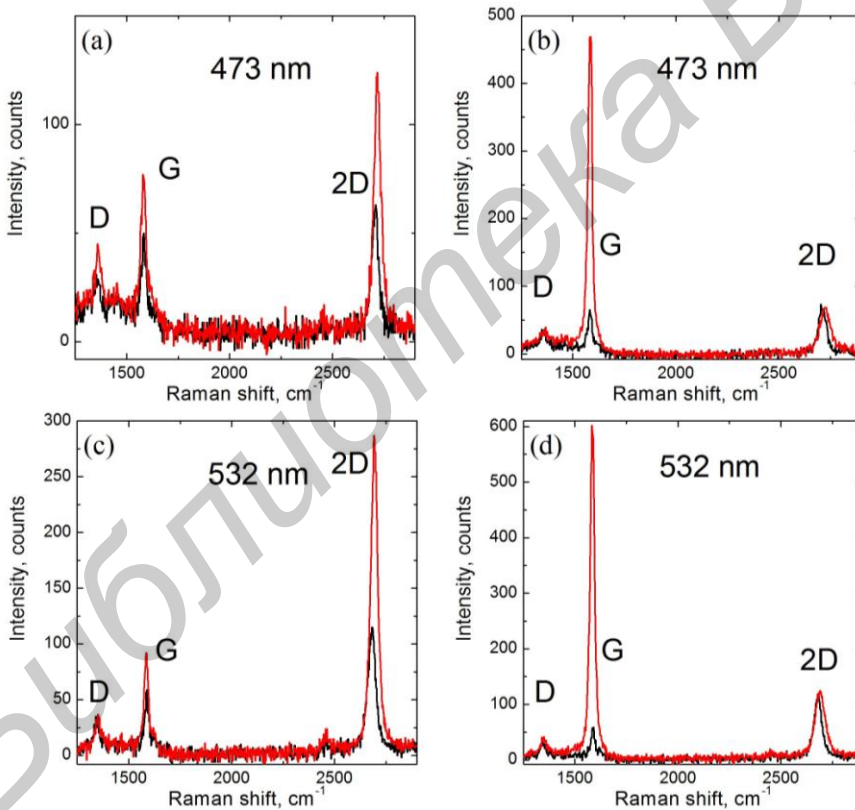
FIGURE 5.13
Raman spectra of sample B on SiO$_2$/Si substrate. (a) Raman spectra of SLG (black) and double layer graphene (red) with the laser excitation wavelength of 532 nm. (b) Raman spectra of SLG (black) and double layer graphene with the G resonance (red) with the laser excitation wavelength of 532 nm. (c) Raman spectra of SLG (black) and double layer graphene with the G resonance (red) with the laser excitation wavelength of 473 nm

For the domains corresponding to the spectra presented in Figures 5.13b and 5.13d it is possible to evaluate the rotation angle θ. Indeed, for small θ values one get [46]

(2) $\theta \approx \frac{3aE_{laser}}{4\pi\hbar v_F}$,

where a is the lattice parameter of graphene (2.46 Å), $\hbar$ is the reduced Planck's constant, v_F is the Fermi velocity in monolayer graphene (10^6 m/s) and E_{laser} is the laser energy. Within this approach, we obtain θ = 13.4° and 11.9° for the laser excitation wavelengths of 473 and 532 nm, respectively. The estimated θ values mean that in the investigated domains the layers of graphene could be electronically decoupled [7,8].

The higher G band intensities were observed at different locations within the same probed area for different excitation wavelengths. This fact allows confirming that the presence of G resonance is a consequence of twisted nature of graphene. However, the ratio of integrated G band intensities for the TG double layer and SGL is ~ 60 and ~30 for excitation wavelengths of 532 and 473 nm, respectively [46]. In our case, it is close to 10 for both wavelengths. The G band enhancement factor is sensitive to structural disorder [48]. Therefore,such a difference can be reasonably explained by the presence of nitrogen in the graphene structure (as confirmed by XPS) andaccompanying stress or polycrystalline nature of the studied thin film. Both factors lead to the decrease of the ratio intensity.

It is worth to underline that the above presented Raman mapping has been performed on different sections of samples (not shown here). One of the main result of this study is the uniformity of the samples confirming their macroscopic homogeneity. For sample B we have provided sets of data where SLG fraction was significant (~50%) that helps to evaluate and compare structural properties of SLG and TG. However, for other sets of data the fraction of double layer TG dominates.

We also proved homogeneity directly by the light transmittance measurement of samples transferred on a glass substrate, the diameter of probed area was ~ 0.5 cm. In Figure 5.14 we show the transmittance spectra for both samples recorded in the 400-800 nm range. It follows from Figure 5.14 that the transmittance for sample B at 550 nm is 94%, while for sample A it is only 87%. The value of 94% corresponds to the number of graphene layers between 2 (95.5%) and 3 (93.3%) [35]. It is worth mentioning, that twisted nature of graphene slightly increases the absorption of the light [11,12]. This fact could be the reason of a slight discrepancy while evaluating the number of layers from the result of Figure 5.14. Less value of transmittance for sample A confirms its greater thickness with respect to sample B, which is in agreement with the results of optical and Raman investigations, see Figs. 5.2-5.4, 5.6.
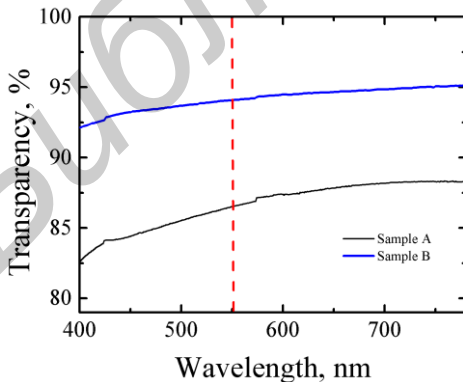

FIGURE 5.14

The transmittance spectra of samples A and B on glass substrate. The vertical dashed line indicates the wavelength at which the transparency was estimated

Impact of the Hydrogen Flow on Structural Properties of Graphene

Now we would like to discuss the two most prominent phenomena observed in our experiments: (i) the morphology change of grown films with hydrogen flow rate and (ii) nitrogen atoms incorporation into graphene. We believe these two phenomena are related to each other. Nevertheless, as a first approach, we will discuss them separately.
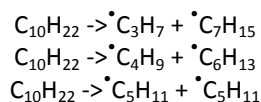
Let us underline the main features that distinguish the morphology of studied samples. The morphology of sample A is characterized by the presence of hexagonally shaped domains with a few and single layer graphene domains. In turn, sample B contains the mixture of single and double layer domains where the double layer fraction dominates. Our studies do not indicate the presence of any regularity in shape and distribution of SLG and double layer domains at measured scale.

Since the hydrogen flow value was the only technological parameter we have varied during the synthesis, we will focus on the impact of hydrogen on the graphene. First of all, the hydrogen partial pressure strongly affects the shape of the graphene edges. It was demonstrated that higher hydrogen pressure favors the hexagonal shape whereas low hydrogen pressure makes dendritic-like growth preferable [49,50]. Our observations, pointed above, are consistent with these findings.

The formation of a few layer graphene requires the formation of the additional graphene layer (layers) on the top or underneath of a SLG. These processes are usually described by wedding cake (WC) [51,52] and inverse wedding cake (IWC) [53,54] models, respectively. Detailed experimental studies strongly support the IWC model of growth [53-55]. It was shown theoretically [56] that the diffusion of C adatoms underneath of existing graphene top layer (GTL) is much faster than on Cu surface free of graphene. Moreover, hydrogen pressure plays crucial role in the growth activity of graphene edges [56]. In particular, low pressure of hydrogen yields the passivation of graphene edges by copper, which prevents the diffusion of C adatoms underneath of GTL and thus contributes to the formation of SLG. Conversely, at high hydrogen pressure the graphene edges are terminated by hydrogen atoms which inhibits the carbon absorption and few layer graphene growth is favored [56]. Considering that double and few layer graphene is really synthesized under our experimental conditions, it is possible to conclude that the partial pressure of hydrogen is still above the threshold of H termination for copper catalyst. In addition, as it was shown in [57] for dendritically shaped graphene single crystals (low partial pressure of hydrogen) multiple small adlayers are favorable. Therefore, we believe that during the $C_{10}H_{22}$ decomposition there is enough amount of hydrogen to terminate the graphene edges [58].

Finally, we turn to the problem of nitrogen incorporation into graphene. Nitrogen can be incorporated into graphene sheet (i) *in situ*, using ammonia as a component of gas carrier mixture [25] or nitrogen containing precursors [59-61] and (ii) by post treatment, e.g., by treatment in ammonia plasma [58] or N ions irradiation [62]. To the best of our knowledge, there is only one article where N_2 gas was used as the nitrogen source during the CVD growth [63]. In our opinion, the main difficulties in using N_2 gas as a nitrogen source arises from the fact that nitrogen molecule possesses of one of the strongest bond with the energy of 226 kcal/mol, which means that the temperature of the CVD process is not enough to decompose significant amount of nitrogen molecules into atoms. The authors of the work [63] did not explore the mechanism of nitrogen incorporation.

We believe that in our case the efficient decomposition of nitrogen occurs due to the presence of hydrocarbon in the reactive mixture. Indeed, as it was shown by C.P. Fenimore, carbon ($^\bullet$C) or hydrocarbon ($^\bullet C_xH_y$) radicals may attack on nitrogen molecules [64]. Endothermicity of such kind of reaction can be an order of magnitude smaller than for a N_2 dissociation process. For example, forthe $^\bullet$CH+N_2=N+$^\bullet$CHN reaction this value was determined as 21.2 ± 0.7 kcal/mol [65]. Moreover,

as it was proved by time-of-flight mass spectrometry experiments, various hydrocarbon radicals can be formed from decane just by thermal decomposition [66]

$$C_{10}H_{22} \rightarrow {}^{\bullet}C_3H_7 + {}^{\bullet}C_7H_{15}$$
$$C_{10}H_{22} \rightarrow {}^{\bullet}C_4H_9 + {}^{\bullet}C_6H_{13}$$
$$C_{10}H_{22} \rightarrow {}^{\bullet}C_5H_{11} + {}^{\bullet}C_5H_{11}$$

However, the issue of the exact reaction route of decane decomposition at elevated temperature over copper catalyst is beyond of our study. We can only reasonably assume that different partial pressure of H_2 in gas mixture could favor some decomposition path. Consequently, it enhances the concentration of radicals with specific configurations. Obviously, the enthalpy of the hydrocarbon reaction with N_2 depends on the hydrocarbon radical configuration [67]. Therefore, using these arguments the variation in doping level for samples A and B could be tentatively explained.

Conclusion

In summary, the graphene films have been studied by micro-Raman technique. Samples have been grown on copper foil by APCVD using decane as a precursor and mixture of nitrogen and hydrogen as a carrier gas with the use of different hydrogen flow rates. A special approach to the Raman data evaluation based on statistical analysis of spectral lines parameters has been developed. This approach allowed associating Raman spectra to fractions of the films with different thicknesses.

Based on the values of the G band and 2D band positions, the double layer fraction of graphene grown with the lower hydrogen feeding rate has been established. Moreover, the elaboration of the Raman spectra revealed the presence of graphene spots with the G-resonance for both excitation wavelengths used in our experiments (473 nm and 532 nm). The observation of the G-resonance directly confirms the twisted nature of graphene. The obtained blue shift of the G and 2D band positions of the SLG fractions is caused by nitrogen doping, which has been proved by the XPS study. Moreover, the binding energy of incorporated nitrogen has been evaluated to be around 402 eV. The level of the G band shift for each sample is consistent with the XPS data. It has been obtained that at the wavelength of 550 nm the transmission coefficient for the film grown with the lower hydrogen feeding rate is equal to 94%, which corresponds to 2-3 graphene layers. This is in good agreement with the micro-Raman findings. We suppose that the variation in the morphology is presumably related to the variation of the hydrogen flow in our experiments, as it has been also demonstrated in by other authors. Finally, the possible mechanism of tolerating of the nitrogen concentration embedded in graphene based on a variety of the endothermicity of a ${}^{\bullet}C_xH_y + N_2$ reaction has been proposed.

Acknowledgements

References

1. Novoselov K. S.,Geim A. K., Morozov S. V., Jiang D., Zhang, Y., Dubonos S. A., Grigorieva I. V., Firsov A. A. *Science*2004, 306, 666-669.
2. Pierucci D., Brumme T., Girard J.-C., Calandra M., Silly M. G., Sirotti F., Barbier A., Mauri F., Ouerghi A.*Sci. Rep*. 2016, 6, No. 33487.
3. Novoselov K. S., McCann E., MorozovS. V., Fal'ko V. I., Katsnelson M. I., Zeitler U., Jiang D., Schedin F., Geim A. K. *Nature Phys*. 2006, 2, 177-180.
4. McCann E., Fal'ko V. I. *Phys. Rev. Lett*. 2006, 96, No. 086805.
5. Adam S., Das Sarma S. *Phys. Rev. B* 2008, 77, No. 115436.
6. Hernandez Y. R., Schweitzer S., Kim J.-S., Kumar Patra A., Englert J., Lieberwirt I.,Liscio A., Palermo V., Feng X., Hirsch A., Kläui M., Müllen K. http://arxiv.org/ftp/arxiv/papers/1301/1301.6087.pdf.
7. de Laissardière G. T., Omid Faizy N., Didier M., Laurence M. *Phys. Rev*. B 2016, 93, No. 235135.
8. Luican A., Guohong L., Reina A., Kong J., Nair R. R., Novoselov K. S., Geim A. K., Andrei E. Y. *Phys. Rev. Lett*. 2011, 106, No. 126802.
9. Brihuega I., Mallet P., González-Herrero H., Trambly de Laissardière G., Ugeda M.M., Magaud L., Gómez-Rodríguez J. M., Ynduráin F., Veuillen J.-Y. *Phys. Rev. Lett*. 2012, 109, No. 196802.
10. Luican-Mayer A., Andrei E. Y. *In: Physics of Graphene* 2014, Aoki H., Dresselhaus M. S. eds. Springer, p. 29-64.
11. Kravets V. G., Grigorenko A. N., NairR. R., Blake P., Anissimova S., Novoselov K. S., Geim A. K. *Phys. Rev. B* 2010, 81, No. 1554138.
12. Yang L., Deslippe J., Park C.-H., Cohen M. L., Louie S. G. *Phys. Rev. Lett*. 2009, 103, No. 186802.
13. Yin L.-J., Qiao J.-B., Zuo W.-J., Li W.-T., He L. *Phys. Rev. B* 2015, 92, No. 081406(R).
14. Cherkez V., de Laissardière G. T., Mallet P., Veuillen J.-Y. *Phys. Rev. B* 2015, 91, No. 155428.
15. Liao L., Wang H., Peng H., Yin J., Koh A. L., Chen Y., Xie Q., Peng H., Liu Z. *Nano Lett*. 2015, 15, 5585-5589.
16. Yan W., He W.-Y., Chu Z.-D., Liu M., Meng L., Dou R.-F., Zhang Y., Liu Z., Nie J.-C., He L. *Nature Commun*. 2013, 4, No. 2159.
17. Nguyen V. H., Nguyen H.-V., Saint-Martin J., Dollfus P. *Nanotechnol*. 2015, 26, No. 115201.
18. Lin Y.-M., Dimitrakopoulos C., Farmer D. B., Han S.-J., Wu Y., Zhu W., Gaskill D. K., Tedesco J. L., Myers-Ward R. L., Eddy C. R., Grill A., Avouris P. *Appl. Phys. Lett*. 2010,97, No. 112107.
19. Lu C.-C., Lin Y.-C., Liu Z., Yeh C.-H., Suenaga K., Chiu P.-W. *ACS Nano* 2013, 7, 2587-2594.
20. Othmen R., Arezki H., Ajlani H., Cavanna A., Boutchich M., Oueslati M., Madouri A. *Appl. Phys. Lett*. 2015, 106, No. 103107.
21. Bae S., Kim H., Lee Y., Xu X., Park J.-S., Zheng Y., Balakrishnan J., Lei T., Kim H. R., Song Y. I., Kim Y.-J., Kim K. S., Özyilmaz B., Ahn J.-H., Hong B. H., Iijima S. *Nature Nanotechnol*. 2010, 5, 574-578.
22. Bhaviripudi S., Jia X.,Dresselhaus M. S., Kong J. *Nano Lett*. 2010, 10, 4128-4133.
23. Song W., Jeon C., Kim S. Y., Kim Y., Kim S. H., Lee S.-I., Jung D. S., Jung M. W., An K.-S., Park C.-Y. *Carbon* 2014, 68, 87-94.
24. Zafar Z., Ni Z. H., Wu X., Shi Z. X., Nan H. Y., Bai J., Sun L. T. *Carbon* 2013, 61, 57-62.
25. Wei D., Liu Y., Wang Y., Zhang H., Huang L., Yu G. *Nano Lett*. 2009, 9, 1752-1758.
26. Seah C.-M., Vigolo B., Chai S.-P., Ichikawa S., Gleize J., Le Normand F., Aweke F., Mohamed A. R. *Carbon* 2016, 96, 268-275.
27. Ishigami M., Chen J., Cullen W., Fuhrer M., Williams E. *Nano Lett*. 2007, 7, 1643-1648.

28. Huang P. Y., Ruiz-Vargas C. S., van der Zande A. M., Whitney W. S., Levendorf M. P., Kevek J. W., Garg S., Alden J. S., Hustedt C. J., Zhu Y., Park J., McEuen P. L., Muller D.A. *Nature* 2011, 469, 389-392.

29. Koepke J. C., Wood J. D., Estrada D., Ong Z.-Y., He K. T., Pop E., Lyding J. W. *ACS Nano* 2013, 7, 75-86.

30. Wood J. D., Doidge G. P., Carrion E. A., Koepke J. C.,Kaitz J. A., Datye I., Behnam A., Hewaparakrama J., Aruin B., Chen Y., Dong H., Haasch R. T., Lyding J. W., Pop E. *Nanotechnology* 2015, 26, No. 055302.

31. Ferrari A. C., Basko D. M. *Nature Nanotechnol*. 2013, 8, 235-246.

32. Losurdo M., Giangregorio M. M., Capezzuto P., Bruno G. *Phys. Chem. Chem. Phys*. 2011, 13, 20836-20843.

33. Costa S. D., Righi A., Fantini C., Hao Y., Magnuson C., Colombo L., Ruoff R. S., Pimenta M. A. *Solid State Commun*. 2012, 152, 1317-1320.

34. Ferrari A. C. *Solid State Commun*. 2007, 143, 47-57.

35. Ferrari A., Meyer J., Scardaci V., Casiraghi C., Lazzeri M., Mauri F., Piscanec S., Jiang D., Novoselov K. S., Roth S., Geim A. K. *Phys. Rev. Lett*. 2006, 97, No. 187401.

36. Lazzeri M., Mauri F. *Phys. Rev. Lett*. 2006, 97, No. 266407.

37. PimentaM. A., Dresselhaus G., Dresselhaus M. S., Cancado L. G., Jorioa A., Saitoe R. *Phys. Chem. Chem. Phys*. 2007, 9 (11), 1276-1291.

38. Cancado L. G., Jorio A., Martins Ferreira E. H., Stavale F., Achete C. A., Capaz R. B., Moutinho M. V. O., Lombardo A., Kulmala T. S., Ferrari A. C. *Nano Lett*. 2011, 11, 3190-3196.

39. Wang Y. Y., Ni Z. H., Shen Z. X., Wang H. M., Wu Y. H. *Appl. Phys. Lett*. 2008, 92, No. 043121.

40. Yoon D., Moon H., Cheong H., Choi J.S., Choi J.A., Park B. H. *J. of Korean Physics Society 2009, 55 (3),1299-1303.*

41. Das A., Pisana S., Chakraborty B., Piscanec S., Saha S.,Waghmare U., Novoselov K. S., Krishnamurthy H. R., Geim A. K., Ferrari A. C., Sood A. K. *Nature Nanotechnol*. 2008, 3, 210-215.

42. Kiuchi H., Kondo T., Sakurai M., Guo D., Nakamura J., Niwa H., Miyawaki J., Kawai M., Oshima M., Harada Y. *Phys. Chem. Chem. Phys.* 2016, 18 , 458-465.

43. Le Normand F., Hommet J., Szorenyi T., Fuchs C., Fogarassy E. *Phys. Rev.* B 2001, 64, No. 235416.

44. Schiros T., Nordlund D., Palova L., Prezzi D., Zhao L., Kim K. S., Wurstbauer U., Gutiérrez C., Delongchamp D., Jaye C., Fischer D., Ogasawara H., Pettersson L. G., Reichman D. R., Kim P., Hybertsen M.S., Pasupathy A. N. *Nano Lett*. 2012, 12 (8), 4025-4031.

45. Reddy A. L. M., Srivastava A., Gowda S. R., Gullapalli H., Dubey M., Ajayan P.M. *ACS Nano* 2010, 4, 6337-6342.

46. Kim K., Coh S, Tan L. Z., Regan W., Yuk J. M., Chatterjee E., Crommie M. F., Cohen M. L., Louie S. G., Zettl A. *Phys. Rev. Lett*. 2012, 108, No. 246103.

47. Wang Y., Su Z., Wu W.,Nie S., Lu X., Wang H., McCarty K. , Pei S-S., Robles-Hernandez F., Hadjiev V. G., Bao J. *Nanotechnology* 2014, 25, No 335201.

48. 48.Schmucker S. W., Cress C. D., Culbertson J. C., Beeman J. W., Dubon O. D., Robinson J. T. *Carbon* 2015, 93, 250-257.

49. Vlassiouk I., Regmi M., Fulvio P., Dai S., Datskos P., Eres G. *ACS Nano* 2011, 5; No. 6069.

50. Shu H., Chen X., Ta X., Ding F. *ACS Nano* 2012, 6, No. 3243.

51. Robertson A. W., Warner J. H. *Nano Lett*. 2011, 11 (3), 1182-1189.

52. Kalbac M., Frank O., Kavan L. *Carbon* 2012, 50, 3682-3687.

53. Wu B., Geng D., Guo Y., Huang L., Xue Y., Zheng J., ChenJ., Yu G., Liu Y., Jiang L., Hu W. *Adv. Mater*. 2011, 23, No. 3522.
54. Nie S., Wu W., Xing S. R., Yu Q. K., Bao J. M., Pei S. S., McCartyK. F. *New J. Phys*. 2012, 14, No. 093028.
55. Li Q., Chou H., Zhong J.-H., Liu J.-Y., Dolocan A., Zhang J., Zhou Y., Ruoff R. S., Chen S., Cai W. *Nano Lett*. 2013, 13 (2), 486-490.
56. Zhang X., Wang L., Xin J., Yakobson B. I., Ding F. J. *Am. Chem. Soc*. 2014, 136, 3040-3047.
57. Zhao P., Cheng Yu, Zhao D., Yin K., Zhang X., Song M., Yin S., Song Y., Wang P., Wang M., Xia Y., Wang H. *Nanoscale* 2016, 8, 7646-7653.
58. Komissarov I. V., Kovalchuck N. G., Kolesov E. A., Tivanov M. S., Korolik O. V., Mazanik A. V., Shaman Yu. P., Basaev A. S., Labunov V. A., Prischepa S. L., Kargin N. I., Ryzhuk R. V., Shostachenko S. A. *Physics Procedia* 2015, 72, 450-454.
59. Jin Z., Yao J., Kittrell C., Tour J. M. *ACS Nano* 2011, 5, 4112.
60. Capasso A., Dikonimos T., Sarto F., Tamburrano A., De Bellis G., Sabrina Sarto M., Faggio G., Malara A., Messina G., Lisi N. *Beilstein J. Nanotechnol*. 2015, 6, 2028-2038.
61. Rybin M., Pereyaslavtsev A., Vasilieva T., Myasnikov V., Sokolov I., Pavlova A., Obraztsova Ekaterina, Khomich A., Ralchenko V., Obraztsova Elena. *Carbon* 2016, 96, 196-202.
62. Sforzini J., Hapala P., Franke M., van Straaten G., Stöhr A., Link S., Soubatch S., Jelínek P., Lee T.-L., Starke U., Švec M., Bocquet F. C., Tautz F. S. *Phys. Rev. Lett*. 2016, 116, No. 126805.
63. Urban J. M., Dabrowski P., Binder J., Kopciuszyński M., Wysmołek A., Klusek Z., Jałochowski M., Strupiński W., Baranowski J. M. *J. Appl. Phys*. 2014, 115, No. 233504.
64. Fenimore C.P. Formation of nitrogen oxide in premixed hydrocarbon flame In *Proceedings of the Combustion Institute* 1971, 13(1), 373-380.
65. Bise R. T., Choi H. S., Neumark D. M. *J. Chem. Phys*. 1999, 111 (11), 4923-4932.
66. Lemieux J. M. Thermal Decomposition of Molecules Relevant to Combustion and Chemical Vapor Deposition by Flash Pyrolysis Time-of-Flight Mass Spectrometry. Ph. D. Thesis, University of Riverside, USA, 2013.
67. Berman M. R., Lin M. C. *J. Phys. Chem*. 1983, 87(20), 3933-3942.

List of symbols	List of acronyms
θ rotation angle between two graphene layers	SLG single layer graphene
n concentration of point defects	TG twisted graphene
n_N average surface concentration of nitrogen atoms	vHS van Hove Singularities
a lattice parameter of graphene	CVD chemical vapor deposition
$\hbar$ reduced Planck`s constant	APCVD atmospheric pressure chemical vapor deposition
ν_F Fermi velocity in monolayer graphene	EDX energy dispersive X-ray
E_{laser} laser energy	PMMA polymethylmethacrylate
	FWHM full width at half maximum
	XPS X-ray photoelectron spectroscopy
	IWC inverse wedding cake
	WC wedding cake
	GTL graphene top layer